Large-eddy simulation of NACA65 compressor cascade with roughness

By J. Joo†, M. Emory‡, S. T. Bose‡, G. Medic†, F. Ham‡ AND O. P. Sharma†

Large-eddy simulations (LES) over NACA65 compressor cascades with roughness were performed for multiple roughness heights. The experiments show flow separation as airfoil roughness is increased. In LES computations, surface roughness was represented by regularly arranged discrete elements using guidelines from Schlichting, as well as with realistic randomly distributed roughness where k_{rms}/l was simply set to k_s/l, i.e., sandgrain roughness, with no conversion factors from engineering practice. For both of these approaches of defining roughness in wall-resolved LES, the results indicate that specifying an equivalent sandgrain roughness height larger than the one in experiments was required to reproduce the same effects observed in experiments. This highlights the persisting uncertainty with matching the experimental roughness geometry in LES computations, pointing towards surface imaging and digitization as a potential solution. Some initial analysis of flow physics has been conducted with the aim of informing the RANS modeling for roughness.

1. Introduction

Roughness on rotating machinery, such as a compressor or a turbine, has detrimental effects on performance and operability. Skin friction losses increase over the rough surface, but also the boundary layer becomes thicker and more prone to separate earlier in presence of adverse pressure gradient, further decreasing efficiency and stall margin.

From a designer's point of view, the understanding and prediction of flow separation induced by roughness are important. Based on such predictions, an admissible blade loading could be determined, where the designer's objective is to design blade shapes that prevent or control flow separation under a roughened surface, which often augments during service.

The early experimental work on this problem was conducted by Bammert & Milsch (1972), where measurements of flow over systematically roughened NACA65 compressor cascades were performed in a low-speed tunnel. The tests showed that the boundary layers start to separate as blades get roughened and the separation locations differ for different blade airfoil curvature and the corresponding pressure loading distributions. Also, the losses were compared for various roughness heights for each airfoil.

Song & Eaton (2002) also demonstrated the trend that roughness promotes the boundary layer separation. In that experiment, the boundary layer that has developed over a rough flat plate creates a substantially larger separation bubble in the backward-facing ramp located downstream of it than in the one that developed over a smooth surface. Roughness models in RANS framework have not been able to consistently predict the roughness-induced separation. Although the two-layer k-epsilon-based rough wall modification by Durbin *et al.* (2001) closely predicted the separation trend in Song & Eaton

† United Technologies Research Center
‡ Cascade Technologies, Inc.

(2002), other widely used roughness models by Wilcox (2004) and Knopp *et al.* (2009) – which is a k-omega-based formulation of the model of Durbin *et al.* (2001), were not able to predict the roughness-induced separation in Bammert's experiment. The key mechanism driving the roughness-induced separation is not well understood, nor is the reason why the conventional roughness modifications of RANS models fail to predict the separation.

Recent LES study of a roughened low-pressure turbine cascade elucidates the process of separation (Joo *et al.* 2016) to some degree. That study is based on experimental data, where the flow over the roughened P&W low-pressure turbine cascade separates as Reynolds number increases. The roughness effects increase as Reynolds number becomes larger – since the roughness height in wall units increases. LES computations predicted the roughness-induced separation and showed that as Reynolds number increases, form drag over the roughness elements also increases, owing to enhanced turbulence mixing and momentum transfer into the roughness sublayer. Conventional turbulence models could not predict the increase of skin-friction and separation, because the formulation to represent such a complex interaction between turbulence mixing and peaks and valleys of the roughness was lacking.

That LES study modeled the roughness as a staggered array of three-dimensional rectangular roughness elements, which is compatible to a block-structured Navier-Stokes solver. The configuration of the array followed Schlichting (1968)'s regularly spaced roughness element table, where sets of different spaces and dimensions are related to equivalent sandgrain roughness values.

The current study focuses on the compressor experiments of Bammert & Milsch (1972). The practice of using an array of discrete roughness elements following Schilchting's guidelines needs to be further assessed for more applications to assess its viability. And the data of Bammert's experiment show that the blade loadings are changing quite substantially with the gradual increase in roughness height, implying that these compressor cascade experiments would be a more challenging problem.

The uncertainty of reproducing the correct equivalent sandgrain roughness height through a certain discrete roughness element configuration clearly leads to a substantial uncertainty with LES or even DNS studies, even though all relevant scales are resolved. To circumvent the problem, one can grid realistic surface roughness, obtained from surface imaging and digitization using unstructured grids. As a pilot study for such an approach, stochastically generated random surface roughness is gridded and solved with an unstructured flow solver.

2. Numerical Method

The block-sturctured LES flow solver that used for this study is based on second-order central difference and second-order accurate implicit method with dual time-stepping. At each inner-iteration, the flow solution is integrated by the Lax-Wendroff explicit time-marching scheme with a multi-grid designed for compressible flow. The core of the solver (Ni 1982) has been extensively validated for turbomachinery over the past 30 years. In the LES framework, the WALE model is employed for subgrid-scale eddy viscosity.

By using the second-order central difference scheme, high wavenumber errors of grid-wise scale tend to accumulate. A low-pass filtering (Lele 1992) was implemented as in Joo (2008), and this can be applied periodically to remove the high-frequency numerical

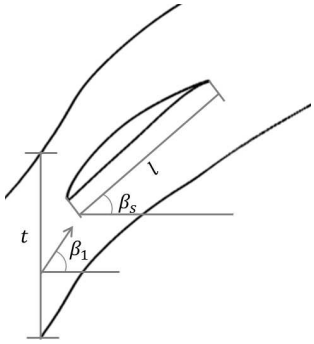

FIGURE 1. Cascade configuration; c: chord, t: pitch, β_s: staggered angle, β_1 inflow angle.

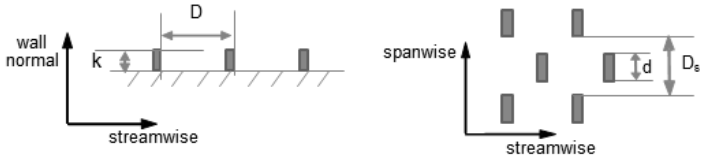

FIGURE 2. Schematic of discrete roughness element configuration.

instabilities when necessary. Details of filtering implementation are explained in Medic *et al.* (2014).

The flow solver used for realistic random distributed roughness is Cliff – an incompressible unstructured N-S solver in CharLES suite developed at Cascade Technologies, Inc.. Detailed information regarding numerical discretization can be found in Khalighi *et al.* (2011) and Bres *et al.* (2013). The Vreman subgrid-scale model (Vreman 2004) is used for LES.

3. Computational setup

A cascade of NACA 65-12(10) airfoil with solidity (t/l) of 1, where t is the pitch and l is the chord length as defined by Bammert & Milsch (1972), was chosen for simulations as the most representative test case. Its stagger and flow angle are defined in Figure 1 as 130 degree and 142.5 degree, respectively, making the angle of attack 12.5 degree. The inlet Mach number is 0.11 and the Reynolds number based on chord length and inlet flow condition is 430,000. The size of the computational domain is such that the inflow boundary is located 1.57 axial chord length upstream from the leading edge and the outflow boundary is at 1.22 axial chord length downstream from the trailing edge. The spanwise domain size is 0.2 chord length. The periodic boundary condition is used for the pitch-wise and span-wise boundaries.

Overall schematic and parameter definitions are drawn in Figure 2. There are three different configurations considered, as shown in Table 1. Cases 1 and 2 targeted the sandgrain roughness heights of $k_s/l = 3.22 \times 10^{-3}$ and 5.56×10^{-3}, respectively. Due to the periodicity and grid resolution requirement in the span-wise direction, the exact representation of Schlichting's configuration No. 15 of Figure 17.10 in Schlichting (1968), where $k = 1.031k_s$, $D = 13.745k$, $D_s = 11k$, $d = 2.75k$,and $d/D_s = 0.25$, is difficult. As the spanwise length of rectangles and spacing are increased, their ratios were maintained as close as possible. In such way, roughness densities and, consequently, the

	Expected k_s/l	k/l	D/k	D_s/k	d/k	d/D_s
Case 1	3.22×10^{-3}	3.22×10^{-3}	13.75	12.37	3.15	0.255
Case 2	5.56×10^{-3}	5.56×10^{-3}	13.75	9.56	2.44	0.255
Case 3	3.43×10^{-3}	7.85×10^{-4}	13.75	7.97	5.97	0.749
Case 4	1.25×10^{-1}	5.56×10^{-3}	6.88	2.25	9.84	4.37

TABLE 1. Roughness configuration parameters; expected sandgrain roughness obtained by Schlichting (1968) for cases 1 and 2 and by Waigh & Kind (1998) for cases 3 and 4.

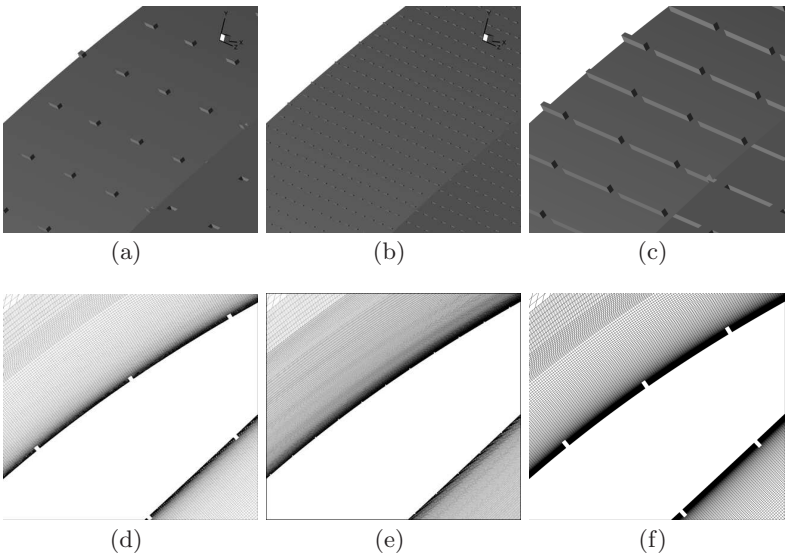

FIGURE 3. Geometry of distributed roughness element; (a), (d) case 1; (b), (e) case 3; (c), (f) case 4.

equivalent roughness height, remain close to the guidelines from Schlicthing. Note that the streamwise spacing is kept the same.

Following this roughness configuration, the heights of roughness element in cases 1 and 2 are chosen to match the corresponding experimental sandgrain roughness heights.

Based on Schlicthings guidelines, case 3 is configured such that the roughness height is lower than its equivalent sandgrain roughness height, but discrete elements are more densely populated, making its equivalent roughness equal to that of case 1 by following the correlation in Waigh & Kind (1998), where a roughness constant – the shifting in log layer – is correlated using different spacing and shape parameters.

The case 4 is configured after obataining the result of case 2, which did not produce enough roughness effects as initially estimated by Schlichting (1968). In case 4, roughness height is kept as in case 2, but streamwise spacing and spanwise spacing are reduced by 0.5 and 3.54 times, respectively. The increased roughness density can be seen in Fig. 3(c). The correlation by Waigh & Kind (1998) indicates about 22.5 times higher sandgrain roughness than the targeted one of $k_s/l = 5.56 \times 10^{-3}$. However, the result of case 4 implies that the real roughness effect in this compressor configuration is substantially

lower – the blade loading of case 4 closely matches the Bammert's $k_s/l = 5.56 \times 10^{-3}$ data.

The total numbers of grid points for cases 1 and 2 are 218 million and for cases 3 and 4, 50 million grid points. Case 1 has denser near-wall resolution since the scale of roughness elements is smaller than in cases 2 and 3. The sizes of C-grid wrapping around the blade are 4672 by 152 by 256 (surface direction, wall-normal direction and spanwise direction) for case 1 and 1167 by 152 by 128 for cases 2 and 3. The size of the latter C-grid is very close to that of the O-grid used for LES of NACA65 cascades in Medic *et al.* (2016), which was 1035 by 72 by 120.

Guidelines for grid resolution for this type of roughness cannot be fully established until a systematic grid refinement study has been performed. One can infer that if roughness height is significant and elements are densely populated, then resolving the shear layer and the roughness element scale will be more relevant than the requirements for resolving the near-wall turbulent boundary layer over a smooth surface, which are represented in wall units. Since cases 1 to 2 have high roughness elements and relatively large streamwise spacing, the current resolution of cases 1 and 2, which are well suited for smooth surface turbulence boundary layer, is not expected to be too coarse. Case 3 has overall very fine grids and in terms of inter-roughness resolution, the number of grid points used is similar to that in case 1. All wall-normal grid size is based on the smooth grid criteria such that y+ is targeted to about 0.3.

In the current study, realistic roughness is generated by applying a digital filter to the normal distributed random fluctuation of surface deviation whose σ is one of parameters to determine roughness height. The length scale of the digital filter is adjusted to obtain target rms of surface deviation – k_{rms}. As seen in Figure 4, two different roughness heights are modeled – $k_{rms}/l = 5.56 \times 10^{-3}$ and 1.56×10^{-3}. There is a significant uncertainty in relating k_{rms}/l to k_s/l. As an initial approach to this type of case, a simplistic method equating the two is used, and its results are assessed in the next chapter. Note that this setting for roughness results in an equivalent sandgrain roughness that is effectively higher than that of experiments (usually a factor that can take any value between 3 and 10 is used for conversion in engineering practice (Bons 2010)).

The numbers of grid points in these simulations are 15 million and 25 million for the cases of $k_{rms}/l = 5.56 \times 10^{-3}$ and 1.56×10^{-3}, respectively. The large roughness case has about 6-7 points per k_{rms} roughness size and the intermediate case has about 4-5 points. These simulations ran for about 10 to 12 blade flow times (l/U_∞).

3.1. *Result*

Each case with discrete roughness elements is integrated in time for about 6 blade flow times (l/U_∞). The latest snapshots of spanwise-averaged instantaneous pressure loadings do not show any flow changing, except unsteady fluctuation near the trailing edge, indicating that flows are matured. To date, no well-converged temporal statistics have been obtained. Neverthless, spanwise-averaged pressure loading can be used to compare to data and to assess the prediction of flow separation.

Figure 5(a) shows the pressure loading of a smooth case using the k-omega Wilcox model, where C_P is defined as

$$C_P = \frac{(p - p_1)}{q_1}, \tag{3.1}$$

where p_1 and q_1 is the static pressure and the dynamic head at the inflow boundary. The deviation of C_P is visible, as is often seen when the flow angle is not correct. The flow

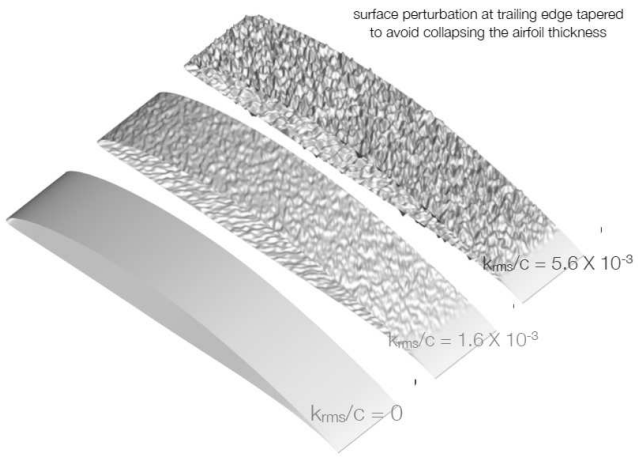

FIGURE 4. Geometry of randomly distributed roughness for unstructured solver

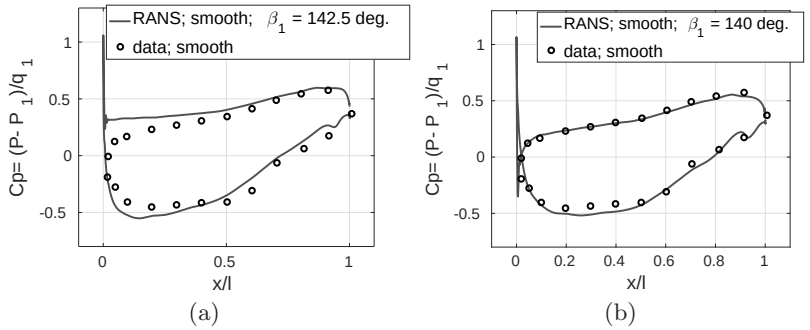

FIGURE 5. Blade loading of smooth blade; (a) default inflow angle, $\beta_1 = 142.5°$, (b) adjusted inflow flow angle, $\beta_1 = 140°$.

angle is typically measured at upstream of the cascade and the three-dimensional effects such as end-wall boundary layer growth can change the actual incidence angle near a leading edge. After adjusting the flow angle by $-2.5°$, the blade loading becomes very close to the experiment data, as shown in Figure 5(b).

The contours of instantaneous Mach number around the roughness elements are shown in Figure 6. Fluctuations between the roughness elements are captured, but a systematic refinement study, however, will be required to verify the results. Figure 6(b) shows the zoomed-out instantaneous Mach contours of the three cases, giving an overall outlook of the simulations.

The spanwise-averaged instantaneous blade loadings are plotted in Figure 7. Although cases 1 and 2 are targeted to the roughness height of $k_s/l \sim 3.22 \times 10^{-3}$ and 5.56×10^{-3}, respectively, their results are closer to the data of $k_s/l = 1.56 \times 10^{-3}$. The spiky structures in the plot are due to local pressure fluctuation due to roughness elements. Flow separation can be inferred from the flattening of blade loading on the suction side. Cases 1 and 2 have very similar pressure loading. From about $x/l \sim 0.7$ on the suction side, case 2 shows a clearer indication of flow separation.

These results question the validity of Schlichting's configuration to generate an equiv-

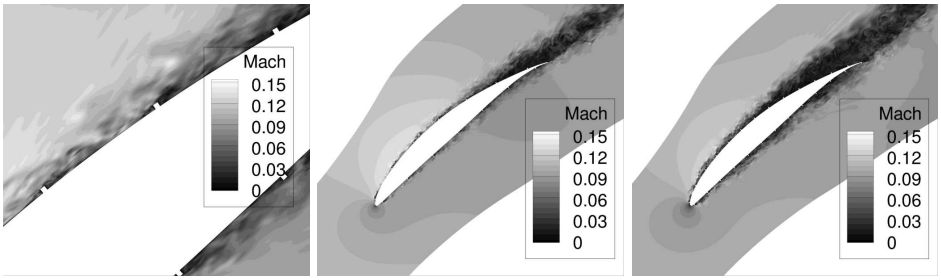

(a) (b) (c)

FIGURE 6. Instantaneous Mach number contours; (a) case 1; (b) case 3; (c) case 2; (d) case 4.

alent sandgrain roughness over an airfoil where the pressure gradient and boundary layer thickness are changing. Based on these simulations, it would appear that the resulting effective roughness is less than what was targeted. In our previous study (Joo *et al.* 2016), the density of roughness elements used in the simulation was higher than the equivalent Schlichting's configuration and the results agreed reasonably well with data, which is consistent with the current result.

The blade loading for case 3 shown in Figure 7(b) looks different from that of case 1, which is supposed to have the equivalent sandgrain roughness, if one follows the correlation in Waigh & Kind (1998). C_P on the pressure side is higher than in the smooth case, which highlights the fact that the near leading edge pressure side C_P of $k_s/l = 0.56\times^{-3}$ case is higher than the smooth data. Although the equivalence of effective roughness may be argued, especially when the boundary layer is thin compared to the roughness height, the interaction between the boundary layer and roughness elements for cases 1 and 3 could be different and may result in a different boundary layer thickness and shape.

The case 4 has the higher density of roughness element and the same height as case 2 and the results show that the blade loading and the flow separation location match well the data of $k_s/l = 5.56\times10^{-3}$. As shown in Tab. 1, the correlation suggests higher effective roughness height. But the effect seems lower, which is consistent with the observations of case 1 to 3.

The blade loadings for the unstructured grid LES computation with realistic roughness cases are shown in Figure 8. The results seem to agree well with the experiment data. For the lower roughness case, the pressure coefficient is not as flat as the data towards the trailing edge on the suction surface, suggesting the flow separation is not fully captured. The higher roughness case shows an excellent agreement with the data.

Note, however, that the realistic random roughness is created to match specified k_{rms}, which is about 0.8 of R_a value – mean absolute deviation of surface displacement – when a normal distribution is used for the random displacement. The conversion factor from R_a to sandgrain roughness can be 2 to 10 (Bons 2010). Given this argument, the equivalent sandgrain roughness heights would be much higher than those of the experimental case that is being used for comparison here.

These results indicate a substantial uncertainty with roughness height definition in the simulations. However, the number of different roughness representations is, as yet, too small to draw a solid conclusion. Also, grid refinement and grid sensitivity studies are needed in the future. Ideally, gridding the exact representation of scanned rough surfaces using unstructured grids would remove the uncertainty. Meanwhile, improving our understanding and characterizing rough surfaces – suitable for a different computational

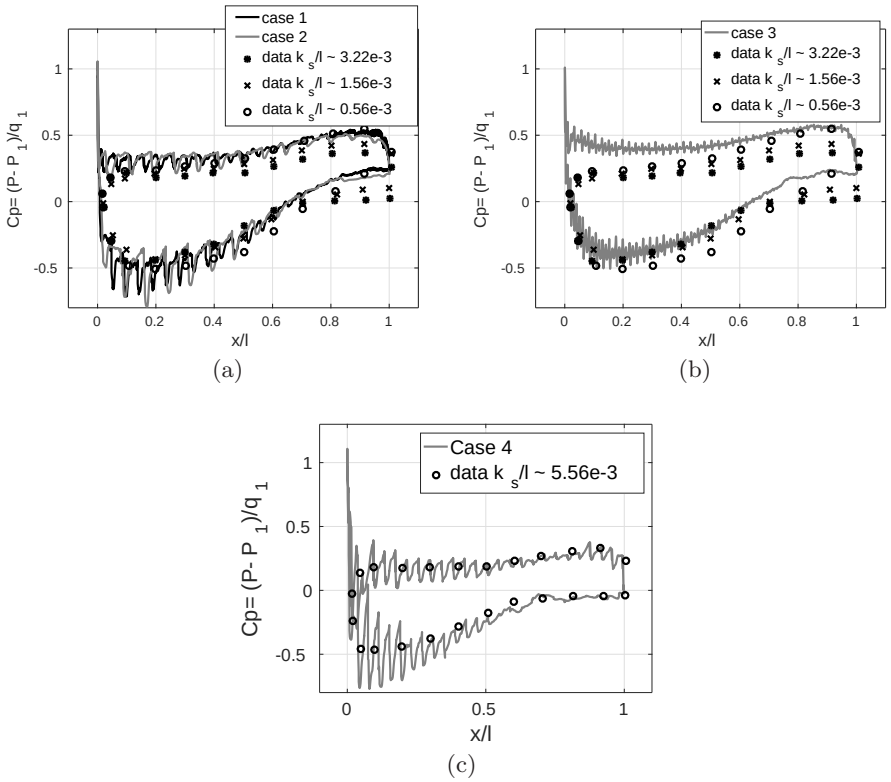

FIGURE 7. Spanwise averaged blade loadings; (a) case 1 and 2; (b) case 3; (c) case 4.

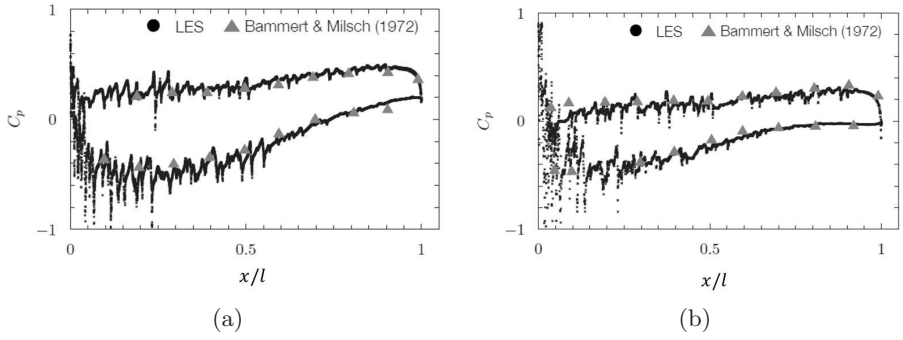

FIGURE 8. Blade loadings of randomly distributed roughness cases; (a) $k_{rms}/l \sim 1.56 \times 10^{-3}$; (b) $k_{rms}/l \sim 5.56 \times 10^{-3}$.

methodology, whether it be still regular discrete elements or realistic random distribution – will build the guiding principle in the future research.

Ultimately, these wall-resolved LES computations should help inform RANS modeling for roughness, particularly with respect to turbulent quantities, where information is often lacking in experiments.

To assess a state-of-the-art roughness RANS model (Knopp *et al.* 2009), spanwise averaged turbulent kinetic energy of case 2 and RANS with Knopp roughness model

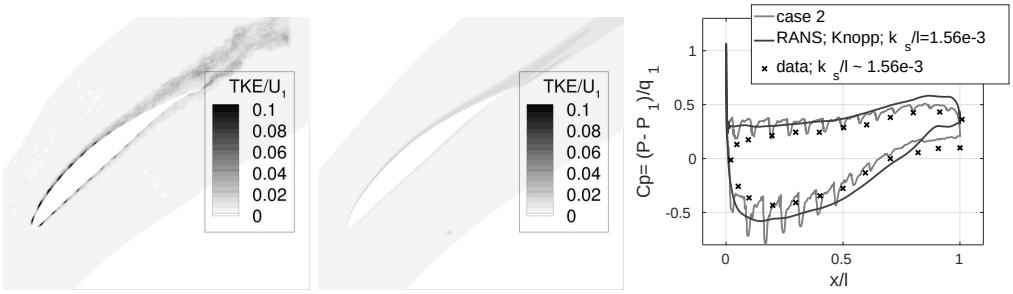

(a) (b) (c)

FIGURE 9. (a), (b) contours of turbulence kinetic energy normalized by flow velocity at inflow of case 2 and RANS with Knopp roughness model with $k_s/l = 1.56 \times 10^{-3}$; (c) blade lodings

with $k_s/l = 1.56 \times 10^{-3}$ are compared, as seen in Figure 9(a,b). Since the blade loading of case 2 is close to Bammert & Milsch (1972)'s data for $k_s/l = 1.56 \times 10^{-3}$, k_s is selected accordingly. RANS simulation produces substantialy lower turbulent kinetic energy, in particular near the wall. This RANS roughness model defines the boundary condition for k as

$$k = u_\tau^2/0.3, \tag{3.2}$$

using observations that in turbulent boundary layers over rough surfaces, the log-layer extends all the way to the wall, and in the log-layer, $\overline{uv}$ is about $0.3k$. While DNS simulations of rough-wall periodic channel flow (Ikeda & Durbin 2007) indicate that this boundary condition may be valid, it is not clear what happens in the boundary layer developing over an airfoil with roughness. With additional results, further comparison of turbulent quantities averaged from LES computations will be made to those of RANS roughness models.

4. Conclusions

Large eddy simulations over NACA65 compressor cascades with roughness were performed for multiple roughness heights. The experiments show flow separation as airfoil roughness is increased. The challenge for LES computations lies in the uncertainty of definition of a proper surface roughness – whether it is represented by regularly arranged discrete elements or realistic randomly distributed roughness. In particular, the question of interest is whether the LES setup will be able to capture the subtle changes in the flow physics with relatively small changes in k_s/l.

As shown previously in Joo *et al.* (2016), if roughness is made large enough, the airfoil will stall. However, matching the exact value of k_s/l is more challenging, whether using guidelines for discrete roughness from Schlichting, or setting the random distribution where k_{rms} has to be set as a fraction of k_s/l. For both these approaches to defining roughness in wall-resolved LES, the results indicate that specifying an equivalent sand-grain roughness height larger than the one in experiments was required to reproduce the same effects observed in experiments. This result highlights the persisting uncertainty with matching the experimental roughness geometry in LES computations, pointing towards surface imaging and digitization as a potential solution.

Some initial comparisons of RANS and LES results have been made, with the objective of understanding the errors in RANS modeling for this class of flows. In particular, of

interest are turbulent quantities in the boundary layer along the suction side for cases with roughness before flow separation occurs. These are usually not well-documented in experiments, thus hindering modeling efforts.

REFERENCES

Bammert, K. & Milsch, R 1972 Boundary layer on rough compressor blades. *ASME* 72-GT-48.

Bons, J. P. 2010 A review of surface roughness effects in gas turbines. *J. Turbomach.* **132**, 021004.

Bres, G. A., Ham, F. E., Nichols, J. W. & Lele, S. K. 2013 Nozzle wall modeling in unstructured large eddy simulations for hot supersonic jet predictions. *AIAA Paper* 2013-2142.

Durbin, P. A., Medic, G., Seo, J.-M., Eaton, J. K. & Song, S. 2001 Rough wall modification of two-layer $k-\epsilon$. *J. Fluids Eng.* **123**, 16–21.

Ikeda, T. & Durbin, P. A. 2007 Direct simulations of a rough-wall channel flow. *J. Fluids Mech.* **571**, 235–263.

Jiménez, J. 2004 Turbulent flows over rough walls. *Annu. Rev. Fluid Mech.* **36**, 173–196.

Joo, J. 2008 *Eddy simulation of turbine blae trailing edge cooling.* Ph.D. Thesis, Stanford University.

Joo, J., Medic, G., & Sharma O. P. 2016 Large-eddy simulation investigation of impact of roughness on flow in a low-pressure turbine. *ASME* GT2016-57912.

Khalighi, Y., Nichols, J. W., Ham, F. E., Lele, S. K. & Moin, P. 2011 Unstructured large eddy simulation for prediction of boise issued from turbulent jets in various configurations. *AIAA Paper* 2011-2886

Knopp, T., Eisfeld, B. & Calvo, J. 2009 A new extension for $k-\omega$ turbulence models to account for wall roughness. *Int. J. Heat Fluid Flow* **30**, 54–65.

Lele, S. K. 1992 Compact finite difference schemes with spectral-like resolution. *J. Comput. Phys.* **103**, 16–43.

Medic, G., Joo, J., Milanovic, I. & Sharma O. P. 2013 Large-eddy simulation for turbine heat transfer. *ASME* GT2014-95841.

Medic, G., Zhang, V., Wang, G., Joo, J., & Sharma O. P. 2016 Prediction of transition and losses in compressor cascades using large-eddy simulation. *J. Turbomach.* **138**, 121001.

Ni, R.-H. 1982 A multiple-grid scheme for solving the Euler equations. *AIAA J.* **20**, 1565–1571.

Schlichting, H. 1968 *Boundary Layer Theory, 6th edition.* McGrow-Hill.

Song, S. & Eaton, J. K. 2002 The effect of wall roughness on the separated flow over a smoothly contoured ramp. *Exp. Fluids.* **33**, 38–46.

Vreman, A. 2004 An eddy-viscosity subgrid-scale model for turbulent shear flow: Algebraic theory and applications. *Phys. Fluids.* **16**, 3670–3682.

Waigh, D. R., & Kind, R. J. 1998 Improved aerodynamic characterization of regular three-dimensional roughness. *AIAA J.* **36**, 1117–1119.

Wilcox D. C. 2004 *Turbulence modeling for CFD*, 2nd edition. DCW Industries.